

Lawrence Berkeley National Laboratory

Lawrence Berkeley National Laboratory

Title

Observation of an Antimatter Hypernucleus

Permalink

<https://escholarship.org/uc/item/1vb8497d>

Author

Abelev, Betty

Publication Date

2010-03-10

Observation of an Antimatter Hypernucleus

B.I.Abelev
(STARCollaboration)
March 10, 2010

*This work was supported by the Director, Office of
Science, Office of Nuclear Science of the U.S.
Department of Energy under Contract No. DE-AC02-
05CH11231.*

Observation of an Antimatter Hypernucleus

The STAR Collaboration

Nuclear collisions recreate conditions in the universe microseconds after the Big Bang. Only a very small fraction of the emitted fragments are light nuclei, but these states are of fundamental interest. We report the observation of antihypertritons - composed of an antiproton, antineutron, and antilambda hyperon - produced by colliding gold nuclei at high energy. Our analysis yields 70 ± 17 antihypertritons (${}^3_{\Lambda}\bar{\text{H}}$) and 157 ± 30 hypertritons (${}^3_{\Lambda}\text{H}$). The measured yields of ${}^3_{\Lambda}\text{H}$ (${}^3_{\Lambda}\bar{\text{H}}$) and ${}^3\text{He}$ (${}^3\bar{\text{He}}$) are similar, suggesting an equilibrium in coordinate and momentum space populations of up, down, and strange quarks and antiquarks, unlike the pattern observed at lower collision energies. The production and properties of antinuclei, and nuclei containing strange quarks, have implications spanning nuclear/particle physics, astrophysics, and cosmology.

Nuclei are abundant in the universe, but antinuclei that are heavier than the antiproton have been observed only as products of interactions at particle accelerators (1, 2). Collisions of heavy nuclei at the Relativistic Heavy-Ion Collider (RHIC) at Brookhaven National Laboratory (BNL) briefly produce hot and dense matter that has been interpreted as a quark gluon plasma (QGP) (3, 4) with an energy density similar to that of the universe a few microseconds after the Big Bang. This plasma contains roughly equal numbers of quarks and antiquarks. As a result of the high energy density of the QGP phase, many strange-antistrange ($s\bar{s}$) quark pairs

are liberated from the quantum vacuum. The plasma cools and transitions into a hadron gas, producing nucleons, hyperons, mesons, and their antiparticles.

Nucleons (protons and neutrons) contain only up and down valence quarks, while hyperons (Λ , Σ , Ξ , Ω) contain at least one strange quark in its 3-quark valence set. A hypernucleus is a nucleus that contains at least one hyperon in addition to nucleons. All hyperons are unstable, even when bound in nuclei. The lightest bound hypernucleus is the hypertriton (${}^3_{\Lambda}\text{H}$), which consists of a Λ hyperon, a proton, and a neutron. The first observation of any hypernucleus was made in 1952 using a nuclear emulsion cosmic ray detector (5). Here, we present the observation of an antimatter hypernucleus.

Production of antinuclei: Models of heavy-ion collisions have had good success in explaining the production of nuclei by assuming that a statistical coalescence mechanism is in effect during the late stage of the collision evolution (4, 6). Antinuclei can be produced through the same coalescence mechanism, and are predicted to be present in cosmic rays. An observed high yield could be interpreted as an indirect signature of new physics, such as Dark Matter (7, 8). Heavy-ion collisions at RHIC provide an opportunity for the discovery and study of many antinuclei and antihypernuclei.

The ability to produce antihypernuclei allows the study of all populated regions in the 3-dimensional chart of the nuclides. The conventional 2-dimensional chart of the nuclides organizes nuclear isotopes in the (N, Z) plane, where N is the number of neutrons and the Z is the number of protons in the nucleus. This chart can be extended to the negative sector in the (N, Z) plane by including antimatter nuclei. Hypernuclei bring a third dimension into play, based on the strangeness quantum number of the nucleus. The present study probes the territory of antinuclei with non-zero strangeness (Fig. 1), where proposed ideas (9–12) related to the structure of nuclear matter can be explored.

Hypernuclei-Formation and observation: The hyperon-nucleon (YN) interaction, respon-

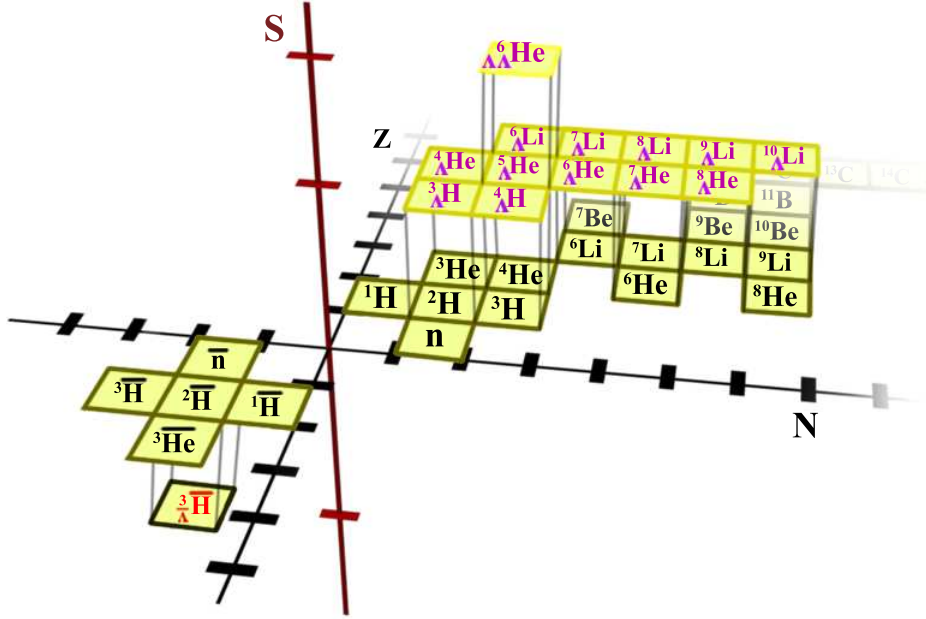


Figure 1: A chart of the nuclides showing the extension into the strangeness sector. Normal nuclei lie in the (N, Z) plane. Antinuclei lie in the negative sector of this plane. Normal hypernuclei lie in the positive (N, Z) quadrant above the plane. The antihypertriton $\bar{\Lambda}^3\bar{H}$ reported here extends this chart into the strangeness octant below the antimatter region in the (N, Z) plane.

sible in part for the binding of hypernuclei, is of fundamental interest in nuclear physics and nuclear astrophysics. For example, the YN interaction plays an important role in attempts to understand the structure of neutron stars. Depending on the strength of the YN interaction, the collapsed stellar core could be composed of hyperons, of strange quark matter, or of a kaon condensate (13). While the hyperons or strange particles inside a dense neutron star would not decay because of local energy constraints, free hypernuclei decay into ordinary nuclei with typical lifetimes of a few hundred picoseconds, which is still thirteen orders of magnitude longer than the lifetimes of the shortest-lived particles. The lifetime of a hypernucleus depends on the strength of the YN interaction (14, 15). Therefore, a precise determination of the lifetime of hypernuclei provides direct information on the YN interaction strength (15, 16).

The experiment was carried out by the STAR collaboration (17) at the RHIC facility. The

main detector of the STAR experiment is a gas-filled cylindrical Time Projection Chamber (TPC), with an inner radius of 50 cm, an outer radius of 200 cm, and a length of 420 cm along the beam line (18). The TPC is a device for imaging, in three dimensions, the ionization left along the path of charged particles. It resolves over 50 million pixels within its active volume. The present analysis is based on interactions produced by colliding two Au beams at an energy of 200 GeV per nucleon-nucleon collision in the center-of-mass system. Approximately 89 million collision events were collected using a trigger designed to accept, as far as possible, all impact parameters (minimum-bias event), and an additional 22 million events were collected using a trigger that preferentially selects near-zero impact parameter (or “head-on”) collisions. The accepted collisions are required to occur within 30 cm of the center of the TPC along the beam line. Charged particle tracks traversing the TPC are reconstructed in an acceptance that is uniform in azimuthal angle. The precise coverage in terms of polar angle is somewhat complicated (18), but roughly speaking, charged tracks emerging at angles with respect to the beam axis in the range of $45^\circ < \theta < 135^\circ$ are reconstructed.

Fig. 2 depicts a typical Au+Au collision reconstructed in the STAR TPC. The tracks are curved by a uniform magnetic field of 0.5 Tesla parallel to the beam line. The event of interest here includes a ${}^3_{\Lambda}\overline{\text{H}}$ candidate created at the primary collision vertex near the center of the TPC. The ${}^3_{\Lambda}\overline{\text{H}}$ travels a few centimeters before it decays. One of the possible decay channels is ${}^3_{\Lambda}\overline{\text{H}} \rightarrow {}^3\overline{\text{He}} + \pi^+$, which occurs with a branching ratio of 25% assuming that this branching fraction is the same as that for ${}^3_{\Lambda}\text{H}$ (15). The two daughter particles then traverse the TPC along with the hundreds of other charged particles produced in the primary Au+Au collision. The trajectories of the daughter particles are reconstructed from the ionization trails they leave in the TPC gas volume (shown in Fig. 2 as thick red and blue lines for ${}^3\overline{\text{He}}$ and π^+ , respectively). The energy loss by these particles to ionization in the TPC, $\langle dE/dx \rangle$, depends on the particle velocity and charge. Particle identification is achieved by correlating the $\langle dE/dx \rangle$ values for charged

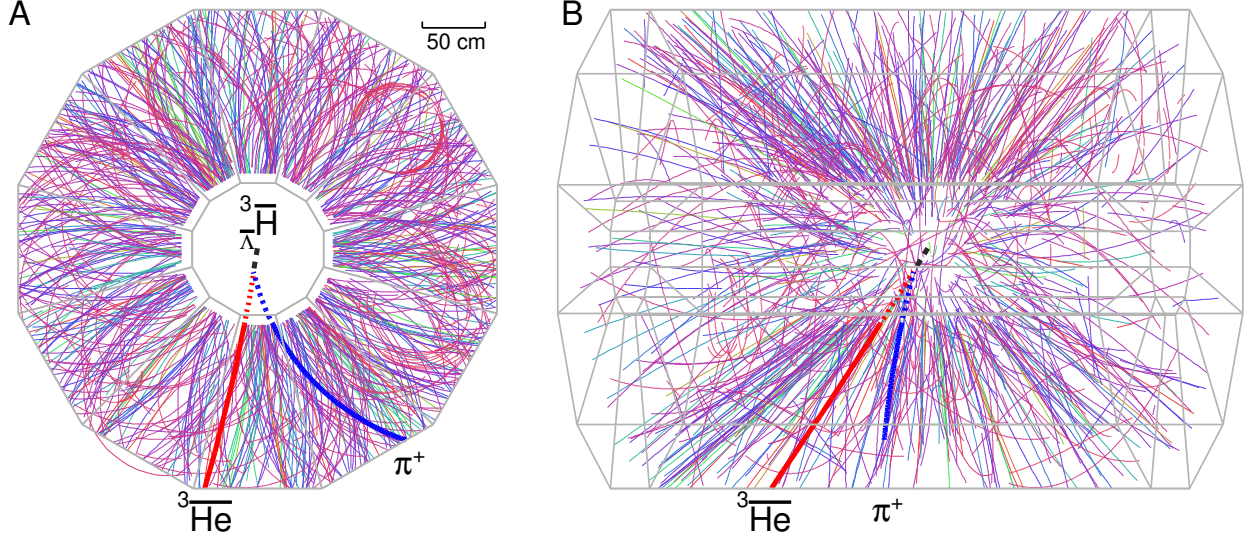


Figure 2: A typical event in the STAR detector that includes the production and decay of a ${}^3_{\Lambda} \overline{H}$ candidate. In (A), the beam axis is normal to the page, and in (B), the beam axis is horizontal. The dashed black line is the trajectory of the ${}^3_{\Lambda} \overline{H}$ candidate, which cannot be directly measured. The heavy red and blue lines are the trajectories of the ${}^3\overline{He}$ and π^+ decay daughters, respectively, which are directly measured.

particles in the TPC with their measured magnetic rigidity, which is proportional to the inverse of the curvature of the trajectory in the magnetic field. With both daughter candidates directly identified, one can trace back along the two helical trajectories to the secondary decay point, and thereby reconstruct the location of the decay vertex as well as the parent momentum vector.

Particle identification: Fig. 3 presents results from the antihypertriton analysis outlined above, along with results from applying the same analysis to measure the normal matter hypertritons in the same dataset — only the sign of the curvature of the decay products is reversed. Fig. 3C shows $\langle dE/dx \rangle$ for negative tracks as a function of the magnetic rigidity; the different bands result from the different particle species. The measured $\langle dE/dx \rangle$ of the particles is compared to the expected value from the Bichsel function (19), which is an extension of the usual Bethe Bloch formulas for energy loss. A new variable, z , is defined as $z = \ln(\langle dE/dx \rangle / \langle dE/dx \rangle_B)$, where $\langle dE/dx \rangle_B$ is the expected value of $\langle dE/dx \rangle$ for the given particle species and momentum. The measured $z({}^3\overline{He})$ distributions for ${}^3\overline{He}$ and ${}^3_{\Lambda} \overline{He}$ tracks

(Fig. 3D), includes 5810 ${}^3\text{He}$ and 2168 ${}^3\overline{\text{He}}$ candidates with $|z({}^3\text{He})| < 0.2$, and represents the largest sample of ${}^3\overline{\text{He}}$ antinuclei that has been collected to date. The first few ${}^3\overline{\text{He}}$ candidates were observed at the Serpukhov accelerator laboratory (20), followed by confirmation from the European Organization for Nuclear Research (CERN) (21). In 2001, a relatively large ${}^3\overline{\text{He}}$ sample was reported by the STAR collaboration (22). The ${}^3\text{He}$ and ${}^3\overline{\text{He}}$ samples in the present analysis are so cleanly identified that misidentification from other weak decays is negligible. However, due to the $\langle dE/dx \rangle$ overlap between ${}^3\text{H}$ and ${}^3\text{He}$ at low momenta, it is only possible to identify the ${}^3\text{He}$ nuclei at relatively high momenta (*i.e.* above ~ 2 GeV/ c). The daughter pions from ${}^3_{\Lambda}\overline{\text{H}}$ decays usually have momenta ~ 0.3 GeV/ c , and can be cleanly identified (23).

Topological reconstruction: A set of topological cuts is invoked in order to identify and reconstruct the secondary decay vertex positions with a high signal-to-background ratio. These cuts involve the distance at the decay vertex between the tracks for the ${}^3\overline{\text{He}}$ and π^+ (< 1 cm), the distance of closest approach (DCA) between the ${}^3_{\Lambda}\overline{\text{H}}$ candidate and the event primary vertex (< 1 cm), the decay length of the ${}^3_{\Lambda}\overline{\text{H}}$ candidate vertex from the event primary vertex (> 2.4 cm), and the DCA between the π track and the event primary vertex (> 0.8 cm). The cuts are optimized based on full detector response simulations (24). Several different cut criteria are also applied to cross-check the results and to estimate the systematic errors. The signal is always present, and the difference in the total yields using different cuts are found to be less than 15%. The total systematic error in the present analysis is 15%.

The parent candidate invariant mass is calculated based on the momenta of the daughter candidates at the decay vertex. The results are shown as the open circles in Fig. 3A for the hypertriton: ${}^3_{\Lambda}\text{H} \rightarrow {}^3\text{He} + \pi^-$, and in Fig. 3B for the antihypertriton: ${}^3_{\Lambda}\overline{\text{H}} \rightarrow {}^3\overline{\text{He}} + \pi^+$. There remains an appreciable combinatorial background in this analysis, which must be described and subtracted. A track rotation method is used to reproduce this background. This approach involves the azimuthal rotation of the daughter ${}^3\text{He}$ (${}^3\overline{\text{He}}$) track candidates by 180 degrees with

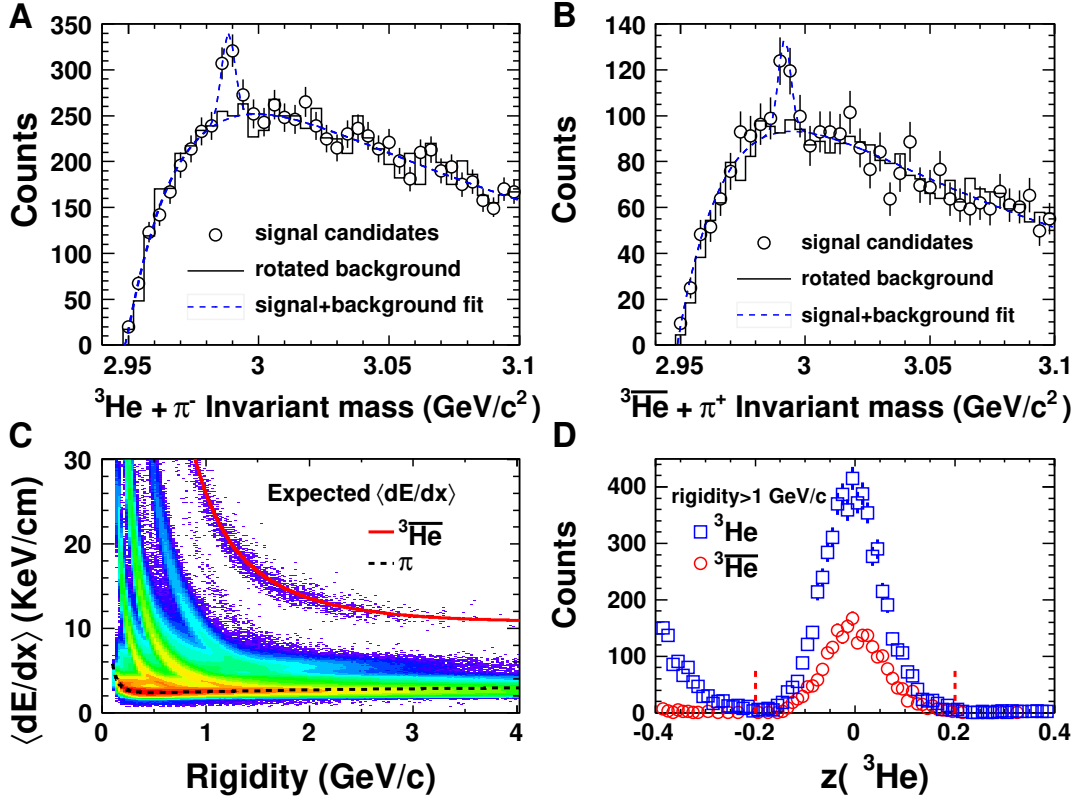


Figure 3: (A, B) show the invariant mass distribution of the daughter ${}^3\text{He} + \pi$. The open circles represent the signal candidate distributions, while the solid black lines are background distributions. The blue dashed lines are signal (Gaussian) plus background (double exponential) combined fit (see the text for details). A (B) shows the ${}^3_\Lambda\text{H}$ (${}^3_\Lambda\bar{\text{H}}$) candidate distributions. (C) shows $\langle dE/dx \rangle$ versus rigidity (momentum/|nuclear charge units|) for negative tracks. Also plotted are the expected values for ${}^3\bar{\text{He}}$ and π tracks. (D) and (C) demonstrate that the ${}^3\text{He}$ and ${}^3\bar{\text{He}}$ tracks ($|z({}^3\text{He})| < 0.2$) are identified essentially without background.

respect to the event primary vertex. In this way, the event is not changed statistically, but all of the secondary decay topologies are destroyed because one of the daughter tracks is rotated away. This provides an accurate description of the combinatorial background. The resulting rotated invariant mass distribution is consistent with the background distribution, as shown by the solid histograms (Fig. 3A,B). The rotated background distribution is fit with a double exponential function: $f(x) \propto \exp(-\frac{x}{p_1}) - \exp(-\frac{x}{p_2})$, where $x = m - m({}^3\text{He}) - m(\pi)$, and p_1, p_2 are fit parameters. Finally, the counts in the signal are calculated after subtraction of this fit function derived from the rotated background. In total, 157 ± 30 ${}^3_\Lambda\text{H}$ and 70 ± 17 ${}^3_\Lambda\bar{\text{H}}$ candidates are thus

observed. The quoted errors are statistical.

Production and properties: We can use the measured ${}^3_{\Lambda}\text{H}$ yield to estimate the expected yield of the ${}^3_{\Lambda}\overline{\text{H}}$, assuming symmetry between matter and antimatter, in the following manner: ${}^3_{\Lambda}\overline{\text{H}} = {}^3_{\Lambda}\text{H} \times {}^3\overline{\text{He}} / {}^3\text{He} = 59 \pm 11$. This indicates a 5.2σ projection of the number of ${}^3_{\Lambda}\overline{\text{H}}$ that is expected in the same data set where ${}^3_{\Lambda}\text{H}$, ${}^3\text{He}$ and ${}^3\overline{\text{He}}$ are detected. An additional check involves fitting the ${}^3\text{He} + \pi$ invariant mass distribution with the combination of a Gaussian “signal” term plus the double-exponential background function (the blue-dashed lines in Fig. 3A,B). The resulting mean values and widths of the invariant mass distributions are consistent with the results from the full detector response simulations. Our best fit values (from χ^2 minimization) are $m({}^3_{\Lambda}\text{H}) = 2.989 \pm 0.001 \pm 0.002 \text{ GeV}/c^2$ and $m({}^3_{\Lambda}\overline{\text{H}}) = 2.991 \pm 0.001 \pm 0.002 \text{ GeV}/c^2$. These values are consistent with each other within the current statistical and systematic errors, and are consistent with the best value from the literature, i.e., $m({}^3_{\Lambda}\text{H}) = 2.99131 \pm 0.00005 \text{ GeV}/c^2$ (16). Our systematic error of $2 \text{ MeV}/c^2$ arises from well-understood instrumental effects that cause small deviations from ideal helical ionization tracks in the TPC.

Lifetimes: The direct reconstruction of the secondary decay vertex in this data allows measurement of the ${}^3_{\Lambda}\text{H}$ lifetime, τ , via the equation $N(t) = N(0)e^{-t/\tau}$, $t = l/(\beta\gamma c)$, $\beta\gamma c = p/m$, where l is the measured decay distance, p is the particle momentum, m is the particle mass, and c is the speed of light. For better statistics in our fit, the ${}^3_{\Lambda}\text{H}$ and ${}^3_{\Lambda}\overline{\text{H}}$ samples are combined, as the matter-antimatter symmetry requires their lifetimes to be equal. Separate measurements of the lifetimes for the two samples show no difference within errors. The signal is then plotted in three bins in $l/\beta\gamma$. The yield in each bin is corrected for the experimental tracking efficiency and acceptance. The total reconstruction efficiency of the ${}^3_{\Lambda}\overline{\text{H}}$ and ${}^3_{\Lambda}\text{H}$ is on the order of 10%, considering all sources of loss and the analysis cuts. The three points are then fit with the exponential function to extract the parameter $c\tau$, and the best-fit result is displayed as the solid line in Fig. 4A. To arrive at the optimum fit, a χ^2 analysis was performed (see the inset to Fig. 4A).

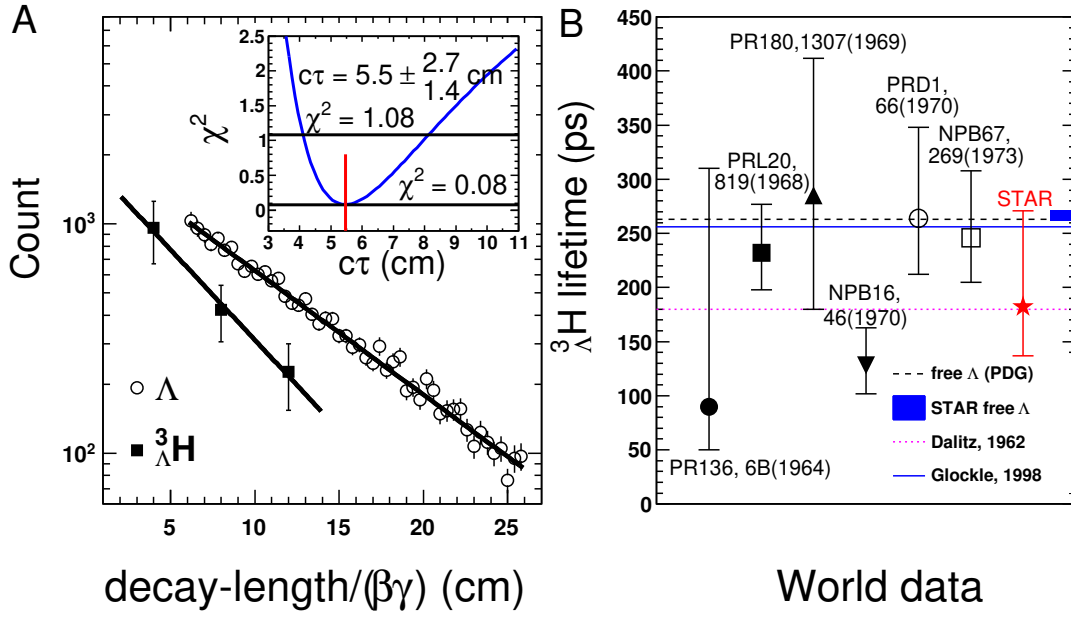


Figure 4: (A) The ³ΛH (solid squares) and Λ (open circles) yield distributions versus $c\tau$. The solid lines represent the $c\tau$ fits. The inset depicts the χ^2 distribution of the best ³ΛH $c\tau$ fit. (B) World data for ³ΛH lifetime measurements. The data points are from Refs. (25–30). The theoretical calculations are from Refs. (14, 15). The error bars represent the statistical uncertainties only.

The $c\tau$ parameter that is observed in this analysis is $c\tau = 5.5 \pm_{1.4}^{2.7} \pm 0.8$ cm, which corresponds to a lifetime τ of $182 \pm_{45}^{89} \pm 27$ ps. As an additional cross-check, the Λ hyperon lifetime is extracted from the same data set using the same approach, for the $\Lambda \rightarrow p + \pi^-$ decay channel. The result obtained is $\tau = 267 \pm 5(stat)$ ps, which is consistent with $\tau = 263 \pm 2$ ps compiled by the Particle Data Group (19).

The ³ΛH lifetime measurements to date (25–31) are not sufficiently accurate to distinguish between models, as depicted by Fig. 4B. The present measurement is consistent with a calculation using a phenomenological ³ΛH wave function (14), and is also consistent with a more recent three-body calculation (15) using a more modern description of the baryon-baryon force. The present result is also comparable to the lifetime of free Λ particles within the uncertainties, and is statistically competitive with the earlier experimental measurements.

Coalescence calculations: The coalescence model makes specific predictions about the ratios of particle yields. These predictions can be checked for a variety of particle species. To

Table 1: Particle ratios from Au+Au collisions at 200 GeV.

Particle type	Ratio
${}^3_{\Lambda}\overline{\text{H}}/{}^3_{\Lambda}\text{H}$	$0.49 \pm 0.18 \pm 0.07$
${}^3\overline{\text{He}}/{}^3\text{He}$	$0.45 \pm 0.02 \pm 0.04$
${}^3_{\Lambda}\overline{\text{H}}/{}^3\overline{\text{He}}$	$0.89 \pm 0.28 \pm 0.13$
${}^3_{\Lambda}\text{H}/{}^3\text{He}$	$0.82 \pm 0.16 \pm 0.12$

determine the invariant particle yields of ${}^3_{\Lambda}\overline{\text{H}}$ and ${}^3_{\Lambda}\text{H}$, corrections for detector acceptance and inefficiency are applied. The ${}^3_{\Lambda}\overline{\text{H}}$ and ${}^3_{\Lambda}\text{H}$ yields are measured in three different transverse momentum (p_t) bins within the analyzed transverse momentum region of $2 < p_t < 6$ GeV/ c and then extrapolated to the unmeasured regions ($p_t < 2$ GeV/ c and $p_t > 6$ GeV/ c). This extrapolation assumes that both ${}^3_{\Lambda}\overline{\text{H}}$ and ${}^3_{\Lambda}\text{H}$ have the same spectral shape as the high-statistics ${}^3\overline{\text{He}}$ and ${}^3\text{He}$ samples from the same data set (see Table 1). If the ${}^3_{\Lambda}\overline{\text{H}}$ and ${}^3_{\Lambda}\text{H}$ are formed by coalescence of $(\bar{\Lambda} + \bar{p} + \bar{n})$ and $(\Lambda + p + n)$, then the production ratio of ${}^3_{\Lambda}\overline{\text{H}}$ to ${}^3_{\Lambda}\text{H}$ should be proportional to $(\frac{\bar{\Lambda}}{\Lambda} \times \frac{\bar{p}}{p} \times \frac{\bar{n}}{n})$. The latter value can be extracted from spectra already measured by STAR, and the value obtained is $0.45 \pm 0.08 \pm 0.10$ (23, 24). The measured ${}^3_{\Lambda}\overline{\text{H}} / {}^3_{\Lambda}\text{H}$ and ${}^3\overline{\text{He}} / {}^3\text{He}$ ratios are consistent with the interpretation that the ${}^3_{\Lambda}\overline{\text{H}}$ and ${}^3_{\Lambda}\text{H}$ are formed by coalescence of $(\bar{\Lambda} + \bar{p} + \bar{n})$ and $(\Lambda + p + n)$, respectively.

Discussion: As the coalescence process for the formation of (anti)hypernuclei requires that (anti)nucleons and (anti)hyperons be in proximity in phase space (i.e., in coordinate and momentum space), (anti)hypernucleus production is sensitive to the correlations in phase-space distributions of nucleons and hyperons (6). An earlier two-particle correlation measurement published by STAR implies a strong phase-space correlation between protons and Λ hyperons (32). Equilibration among the strange quark flavors and light quark flavors is one of the

proposed signatures of QGP formation (33), which would result in high (anti)hypernucleus yields. In addition, recent theoretical studies motivate a search for the onset of QGP by studying the evolution of the baryon – strangeness correlation as a function of collision energy (34–36). The ${}^3_{\Lambda}\text{H}$ yields provide a natural and sensitive tool to extract this correlation (6, 37), as they can be compared to the yields of ${}^3\text{He}$ and ${}^3\text{H}$, which have the same atomic mass number. Besides $4u + 4d$ valence quarks, the valence quark content of these species includes one additional u , d and s quark for ${}^3\text{He}$, ${}^3\text{H}$ and ${}^3_{\Lambda}\text{H}$, respectively. Recent nuclear transport model calculations (37) support the expectation that the strangeness population factor, $S_3 = {}^3_{\Lambda}\text{H}/({}^3\text{He} \times \Lambda/p)$, can be used as a tool to distinguish the QGP from a purely hadronic phase.

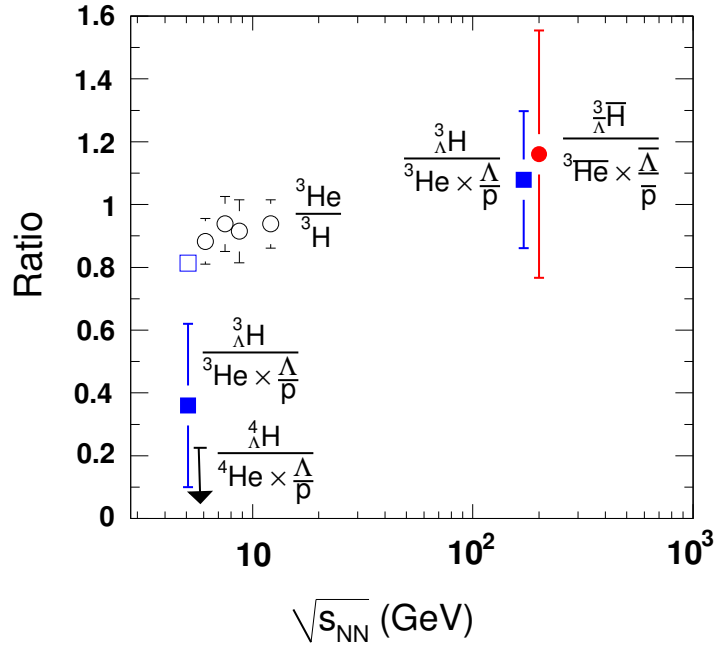


Figure 5: Particle ratios as a function of center-of-mass energy per nucleon-nucleon collision. The data at lower energies are from Refs. (38–40). The ${}^4_{\Lambda}\text{H}/({}^4\text{He} \times \Lambda/p)$ ratio is corrected for the spin degeneracy factor (38). The error bars represent statistical uncertainties only.

Fig. 5 depicts various particle ratios as a function of the collision energy. The ${}^3\text{He}/{}^3\text{H}$ ratio at a center-of-mass energy of 5 GeV obtained at the Alternating Gradient Synchrotron (AGS)

at BNL is much closer to unity than the ratio ${}^3_{\Lambda}\text{H}/{}^3\text{He}$ at the same energy. The values of S_3 are about 1/3 at AGS energies, and near unity at RHIC energies, although with large uncertainties. The AGS value is further constrained to be relatively low by the measured upper limit on the ${}^4_{\Lambda}\text{H}/{}^4\text{He}$ ratio (38), indicating that the phase space population for strangeness is very similar to that for the light quarks in high-energy heavy-ion collisions at RHIC, in contrast to the situation at AGS.

Individual relativistic heavy-ion collisions produce abundant hyperons containing one (Λ , Σ), two (Ξ) or three (Ω) strange (anti)quarks. The coalescence mechanism for hypernucleus production in these collisions thus provides a source for other exotic hypernucleus searches. This should allow an extension of the 3-D chart of the nuclides (Fig. 1) further into the antimatter sectors. Future RHIC running will provide increased statistics, allowing detailed studies of masses and lifetimes, as well as stringent tests of production rates compared to predictions based on coalescence models.

Concluding remark: Evidence for the observation of an antihypernucleus, the ${}^3_{\Lambda}\overline{\text{H}}$, with a statistical significance of 4.1σ has been presented; consistency checks and constraints from a ${}^3_{\Lambda}\text{H}$ analysis in the same event sample, with 5.2σ significance, support this conclusion. The lifetime is observed to be $\tau = 182 \pm_{45}^{89} \pm 27$ ps, which is comparable to that of the free Λ hyperon within current uncertainties. The ${}^3_{\Lambda}\overline{\text{H}}$ (${}^3_{\Lambda}\text{H}$) to ${}^3\overline{\text{He}}$ (${}^3\text{He}$) ratio is close to unity and is significantly larger than that measured at lower beam energies, indicating that the strangeness phase space population is similar to that of light quarks. An order-of-magnitude larger sample of similar collisions is scheduled to be recorded in the near future. The antihypernucleus observation demonstrates that RHIC is an ideal facility for producing exotic hypernuclei and antinuclei.

References

1. J. Alcaraz *et al.*, *Phys. Lett. B* **461**, 387 (1999).

2. H. Fuke *et al.*, *Phys. Rev. Lett.* **95**, 081101 (2005).
3. J. Adams *et al.*, *Nucl. Phys. A* **757**, 102 (2005).
4. P. Braun-Munzinger, J. Stachel, *Nature* **448**, 302 (2007). Also references therein.
5. M. Danysz, J. Pniewski, *Phil. Mag.* **44**, 348 (1953).
6. H. Sato, K. Yazaki, *Phys. Lett. B* **98**, 153 (1981).
7. S. Ahlen *et al.*, *Nucl. Instrum. Methods A* **350**, 351 (1994).
8. F. Donato, N. Fornengo, D. Maurin, *Phys. Rev. D* **78**, 043506 (2008).
9. W. Greiner, *Int. J. Mod. Phys. E* **5**, 1 (1996).
10. U. Heinz, P. R. Subramanian, H. Stöcker, W. Greiner, *J. Phys. G: Nucl. Phys.* **12**, 1237 (1986).
11. C. Greiner, D.-H. Rischke, H. Stöcker, P. Koch, *Phys. Rev. D* **38**, 2797 (1988).
12. J. Schaffner, C. Greiner, H. Stöcker, *Phys. Rev. C* **46**, 322 (1992).
13. J. M. Lattimer, M. Prakash, *Science* **304**, 536 (2004).
14. R. H. Dalitz, G. Rajasekharan, *Phys. Lett.* **1**, 58 (1962).
15. H. Kamada, J. Golak, K. Miyagawa, H. Witala, W. Glöckle, *Phys. Rev. C* **57**, 1595 (1998).
16. M. Juric *et al.*, *Nucl. Phys. B* **52**, 1 (1973).
17. K. H. Ackermann *et al.*, *Nucl. Instrum. Methods A* **499**, 624 (2003).
18. M. Anderson *et al.*, *Nucl. Instrum. Methods A* **499**, 659 (2003).

19. C. Amsler *et al.*, *Phys. Lett. B* **667**, 1 (2008).
20. Y. Antipov *et al.*, *Sov. J. Nucl. Phys.* **12**, 171 (1971).
21. G. Ambrosini *et al.*, *Heavy Ion Phys.* **14**, 297 (2001).
22. C. Adler *et al.*, *Phys. Rev. Lett.* **87**, 262301 (2001).
23. B. I. Abelev *et al.*, *Phys. Rev. Lett.* **97**, 152301 (2006).
24. J. Adams *et al.*, *Phys. Rev. Lett.* **98**, 062301 (2007).
25. R. J. Prem, P. H. Steinberg, *Phys. Rev.* **136**, B1803 (1964).
26. G. Keyes *et al.*, *Phys. Rev. Lett.* **20**, 819 (1968).
27. R. E. Phillips, J. Schneps, *Phys. Rev.* **180**, 1307 (1969).
28. G. Bohm *et al.*, *Nucl. Phys. B* **16**, 46 (1970).
29. G. Keyes *et al.*, *Phys. Rev. D* **1**, 66 (1970).
30. G. Keyes, J. Sacton, J. H. Wickens, M. M. Block, *Nucl. Phys. B* **67**, 269 (1973).
31. M. M. Block *et al.*, *Proceedings of the International Conference on Hyperfragments at St. Cergue 1963*, CERN report 64-1 p. 63 (1964).
32. J. Adams *et al.*, *Phys. Rev. C* **74**, 064906 (2006).
33. J. Rafelski, B. Müller, *Phys. Rev. Lett.* **48**, 1066 (1982).
34. V. Koch, A. Majumder, J. Randrup, *Phys. Rev. Lett.* **95**, 182301 (2005).
35. A. Majumder, B. Müller, *Phys. Rev. C* **74**, 054901 (2006).

36. R. V. Gavai, S. Gupta, *Phys. Rev. D* **73**, 014004 (2006).
37. S. Zhang *et al.*, *Phys. Lett. B* **684**, 224 (2010).
38. T. A. Armstrong *et al.*, *Phys. Rev. C* **70**, 024902 (2004).
39. T. A. Armstrong *et al.*, *Phys. Rev. C* **61**, 064908 (2000).
40. V. I. Kolesnikov for the NA49 Collaboration, *J. Phys. Conf. Ser.* **110**, 032010 (2008).
41. We thank K. Synder for providing Fig. 1. We thank the RHIC Operations Group and RCF at BNL, the NERSC Center at LBNL and the Open Science Grid consortium for providing resources and support. This work was supported in part by the Offices of NP and HEP within the U.S. DOE Office of Science, the U.S. NSF, the Sloan Foundation, the DFG cluster of excellence ‘Origin and Structure of the Universe’, CNRS/IN2P3, STFC and EPSRC of the United Kingdom, FAPESP CNPq of Brazil, Ministry of Ed. and Sci. of the Russian Federation, NNSFC, CAS, MoST, and MoE of China, GA and MSMT of the Czech Republic, FOM and NOW of the Netherlands, DAE, DST, and CSIR of India, Polish Ministry of Sci. and Higher Ed., Korea Research Foundation, Ministry of Sci., Ed. and Sports of the Rep. Of Croatia, Russian Ministry of Sci. and Tech, and RosAtom of Russia.

B. I. Abelev,⁸ M. M. Aggarwal,³¹ Z. Ahammed,⁴⁸ A. V. Alakhverdyants,¹⁸ I. Alekseev,¹⁶ B. D. Anderson,¹⁹ D. Arkhipkin,³ G. S. Averichev,¹⁸ J. Balewski,²³ L. S. Barnby,² S. Baumgart,⁵³ D. R. Beavis,³ R. Bellwied,⁵¹ M. J. Betancourt,²³ R. R. Betts,⁸ A. Bhasin,¹⁷ A. K. Bhati,³¹ H. Bichsel,⁵⁰ J. Bielcik,¹⁰ J. Bielcikova,¹¹ B. Biritz,⁶ L. C. Bland,³ B. E. Bonner,³⁷ J. Bouchet,¹⁹ E. Braidot,²⁸ A. V. Brandin,²⁶ A. Bridgeman,¹ E. Bruna,⁵³ S. Bueltmann,³⁰ I. Bunzarov,¹⁸ T. P. Burton,² X. Z. Cai,⁴¹ H. Caines,⁵³ M. Calderon,⁵ O. Catu,⁵³ D. Cebra,⁵ R. Cendejas,⁶ M. C. Cervantes,⁴³ Z. Chajecki,²⁹ P. Chaloupka,¹¹ S. Chattopadhyay,⁴⁸ H. F. Chen,³⁹ J. H. Chen,⁴¹ J. Y. Chen,⁵² J. Cheng,⁴⁵ M. Cherney,⁹ A. Chikanian,⁵³ K. E. Choi,³⁵ W. Christie,³ P. Chung,¹¹

R. F. Clarke,⁴³ M. J. M. Codrington,⁴³ R. Corliss,²³ J. G. Cramer,⁵⁰ H. J. Crawford,⁴ D. Das,⁵
 S. Dash,¹³ A. Davila Leyva,⁴⁴ L. C. De Silva,⁵¹ R. R. Debbe,³ T. G. Dedovich,¹⁸ M. DePhillips,³
 A. A. Derevschikov,³³ R. Derradi de Souza,⁷ L. Didenko,³ P. Djawotho,⁴³ S. M. Dogra,¹⁷
 X. Dong,²² J. L. Drachenberg,⁴³ J. E. Draper,⁵ J. C. Dunlop,³ M. R. Dutta Mazumdar,⁴⁸ L. G. Efimov,¹⁸
 E. Elhalhuli,² M. Elnimr,⁵¹ J. Engelage,⁴ G. Eppley,³⁷ B. Erasmus,⁴² M. Estienne,⁴² L. Eun,³²
 O. Evdokimov,⁸ P. Fachini,³ R. Fatemi,²⁰ J. Fedorisin,¹⁸ R. G. Fersch,²⁰ P. Filip,¹⁸ E. Finch,⁵³
 V. Fine,³ Y. Fisyak,³ C. A. Gagliardi,⁴³ D. R. Gangadharan,⁶ M. S. Ganti,⁴⁸ E. J. Garcia-Solis,⁸
 A. Geromitsos,⁴² F. Geurts,³⁷ V. Ghazikhanian,⁶ P. Ghosh,⁴⁸ Y. N. Gorbunov,⁹ A. Gordon,³
 O. Grebenyuk,²² D. Grosnick,⁴⁷ B. Grube,³⁵ S. M. Guertin,⁶ A. Gupta,¹⁷ N. Gupta,¹⁷ W. Guryn,³
 B. Haag,⁵ A. Hamed,⁴³ L-X. Han,⁴¹ J. W. Harris,⁵³ J.P. Hays-Wehle,²³ M. Heinz,⁵³ S. Heppelmann,³²
 A. Hirsch,³⁴ E. Hjort,²² A. M. Hoffman,²³ G. W. Hoffmann,⁴⁴ D. J. Hofman,⁸ R. S. Hollis,⁸
 B. Huang,³⁹ H. Z. Huang,⁶ T. J. Humanic,²⁹ L. Huo,⁴³ G. Igo,⁶ A. Iordanova,⁸ P. Jacobs,²²
 W. W. Jacobs,¹⁵ P. Jakl,¹¹ C. Jena,¹³ F. Jin,⁴¹ C. L. Jones,²³ P. G. Jones,² J. Joseph,¹⁹ E. G. Judd,⁴
 S. Kabana,⁴² K. Kajimoto,⁴⁴ K. Kang,⁴⁵ J. Kapitan,¹¹ K. Kauder,⁸ D. Keane,¹⁹ A. Kechechyan,¹⁸
 D. Kettler,⁵⁰ D. P. Kikola,²² J. Kiryluk,²² A. Kisiel,⁴⁹ S. R. Klein,²² A. G. Knospe,⁵³ A. Kocoloski,²³
 D. D. Koetke,⁴⁷ T. Kollegger,¹² J. Konzer,³⁴ M. Kopytine,¹⁹ I. Koralt,³⁰ L. Koroleva,¹⁶ W. Korsch,²⁰
 L. Kotchenda,²⁶ V. Kouchpil,¹¹ P. Kravtsov,²⁶ K. Krueger,¹ M. Krus,¹⁰ L. Kumar,³¹ P. Kurnadi,⁶
 M. A. C. Lamont,³ J. M. Landgraf,³ S. LaPointe,⁵¹ J. Lauret,³ A. Lebedev,³ R. Lednický,¹⁸
 C-H. Lee,³⁵ J. H. Lee,³ W. Leight,²³ M. J. Levine,³ C. Li,³⁹ L. Li,⁴⁴ N. Li,⁵² W. Li,⁴¹ X. Li,³⁴
 Y. Li,⁴⁵ Z. Li,⁵² G. Lin,⁵³ S. J. Lindenbaum,²⁷ M. A. Lisa,²⁹ F. Liu,⁵² H. Liu,⁵ J. Liu,³⁷ T. Ljubicic,³
 W. J. Llope,³⁷ R. S. Longacre,³ W. A. Love,³ Y. Lu,³⁹ T. Ludlam,³ X. Luo,³⁹ G. L. Ma,⁴¹
 Y. G. Ma,⁴¹ D. P. Mahapatra,¹³ R. Majka,⁵³ O. I. Mal,¹⁵ L. K. Mangotra,¹⁷ R. Manweiler,⁴⁷
 S. Margetis,¹⁹ C. Markert,⁴⁴ H. Masui,²² H. S. Matis,²² Yu. A. Matulenko,³³ D. McDonald,³⁷
 T. S. McShane,⁹ A. Meschanin,³³ R. Milner,²³ N. G. Minaev,³³ S. Mioduszewski,⁴³ A. Mischke,²⁸
 M. K. Mitrovski,¹² B. Mohanty,⁴⁸ M. M. Mondal,⁴⁸ B. Morozov,¹⁶ D. A. Morozov,³³ M. G. Munhoz,³⁸

B. K. Nandi,¹⁴ C. Natrass,⁵³ T. K. Nayak,⁴⁸ J. M. Nelson,² P. K. Netrakanti,³⁴ M. J. Ng,⁴
 L. V. Nogach,³³ S. B. Nurushev,³³ G. Odyniec,²² A. Ogawa,³ H. Okada,³ V. Okorokov,²⁶ D. Olson,²²
 M. Pachr,¹⁰ B. S. Page,¹⁵ S. K. Pal,⁴⁸ Y. Pandit,¹⁹ Y. Panebratsev,¹⁸ T. Pawlak,⁴⁹ T. Peitzmann,²⁸
 V. Perevoztchikov,³ C. Perkins,⁴ W. Peryt,⁴⁹ S. C. Phatak,¹³ P. Pile,³ M. Planinic,⁵⁴ M. A. Ploskon,²²
 J. Pluta,⁴⁹ D. Plyku,³⁰ N. Poljak,⁵⁴ A. M. Poskanzer,²² B. V. K. S. Potukuchi,¹⁷ C. B. Powell,²²
 D. Prindle,⁵⁰ C. Pruneau,⁵¹ N. K. Pruthi,³¹ P. R. Pujahari,¹⁴ J. Putschke,⁵³ R. Raniwala,³⁶
 S. Raniwala,³⁶ R. L. Ray,⁴⁴ R. Redwine,²³ R. Reed,⁵ H. G. Ritter,²² J. B. Roberts,³⁷ O. V. Rogachevskiy,¹⁸
 J. L. Romero,⁵ A. Rose,²² C. Roy,⁴² L. Ruan,³ R. Sahoo,⁴² S. Sakai,⁶ I. Sakrejda,²² T. Sakuma,²³
 S. Salur,²² J. Sandweiss,⁵³ E. Sangaline,⁵ J. Schambach,⁴⁴ R. P. Scharenberg,³⁴ N. Schmitz,²⁴
 T. R. Schuster,¹² J. Seele,²²³ J. Seger,⁹ I. Selyuzhenkov,¹⁵ P. Seyboth,²⁴ E. Shahaliev,¹⁸ M.
 Shao,³⁹ M. Sharma,⁵¹ S. S. Shi,⁵² E. P. Sichtermann,²² F. Simon,²⁴ R. N. Singaraju,⁴⁸ M. J. Skoby,³⁴
 N. Smirnov,⁵³ P. Sorensen,³ J. Sowinski,¹⁵ H. M. Spinka,¹ B. Srivastava,³⁴ T. D. S. Stanislaus,⁴⁷
 D. Staszak,⁶ J.R. Stevens,¹⁵ R. Stock,¹² M. Strikhanov,²⁶ B. Stringfellow,³⁴ A. A. P. Suaide,³⁸
 M. C. Suarez,⁸ N. L. Subba,¹⁹ M. Sumbera,¹¹ X. M. Sun,²² Y. Sun,³⁹ Z. Sun,²¹ B. Surrow,²³
 D. N. Svirida,¹⁶ T. J. M. Symons,²² A. Szanto de Toledo,³⁸ J. Takahashi,⁷ A. H. Tang,³ Z.
 Tang,³⁹ L. H. Tarini,⁵¹ T. Tarnowsky,²⁵ D. Thein,⁴⁴ J. H. Thomas,²² J. Tian,⁴¹ A. R. Timmins,⁵¹
 S. Timoshenko,²⁶ D. Tlusty,¹¹ M. Tokarev,¹⁸ T. A. Trainor,⁵⁰ V. N. Tram,²² S. Trentalange,⁶
 R. E. Tribble,⁴³ O. D. Tsai,⁶ J. Ulery,³⁴ T. Ullrich,³ D. G. Underwood,¹ G. Van Buren,³ M. van Leeuwen,²⁸
 G. van Nieuwenhuizen,²³ J. A. Vanfossen, Jr.,¹⁹ R. Varma,¹⁴ G. M. S. Vasconcelos,⁷ A. N. Vasiliev,³³
 F. Videbaek,³ Y. P. Viyogi,⁴⁸ S. Vokal,¹⁸ S. A. Voloshin,⁵¹ M. Wada,⁴⁴ M. Walker,²³ F. Wang,³⁴
 G. Wang,⁶ H. Wang,²⁵ J. S. Wang,²¹ Q. Wang,³⁴ X. L. Wang,³⁹ Y. Wang,⁴⁵ G. Webb,²⁰ J. C. Webb,⁴⁷
 G. D. Westfall,² C. Whitten Jr.,⁶ H. Wieman,²² E. Wingfield,⁴⁴ S. W. Wissink,¹⁵ R. Witt,⁴⁶
 Y. Wu,⁵² W. Xie,³⁴ N. Xu,²² Q. H. Xu,⁴⁰ W. Xu,⁶ Y. Xu,³⁹ Z. Xu,³ L. Xue,⁴¹ Y. Yang,²¹ P.
 Yepes,³⁷ K. Yip,³ I-K. Yoo,³⁵ Q. Yue,⁴⁵ M. Zawisza,⁴⁹ H. Zbroszczyk,⁴⁹ W. Zhan,²¹ J. Zhang,⁵²
 S. Zhang,⁴¹ W. M. Zhang,¹⁹ X. P. Zhang,²² Y. Zhang,²² Z. P. Zhang,³⁹ J. Zhao,⁴¹ C. Zhong,⁴¹ J.

Zhou,³⁷ W. Zhou,⁴⁰ X. Zhu,⁴⁵ Y. H. Zhu,⁴¹ R. Zoulkarneev,¹⁸ Y. Zoulkarneeva,¹⁸

¹Argonne National Laboratory, Argonne, Illinois 60439, USA

²University of Birmingham, Birmingham, United Kingdom

³Brookhaven National Laboratory, Upton, New York 11973, USA

⁴University of California, Berkeley, California 94720, USA

⁵University of California, Davis, California 95616, USA

⁶University of California, Los Angeles, California 90095, USA

⁷Universidade Estadual de Campinas, Sao Paulo, Brazil

⁸University of Illinois at Chicago, Chicago, Illinois 60607, USA

⁹Creighton University, Omaha, Nebraska 68178, USA

¹⁰Czech Technical University in Prague, FNSPE, Prague, 115 19, Czech Republic

¹¹Nuclear Physics Institute AS CR, 250 68 Řež/Prague, Czech Republic

¹²University of Frankfurt, Frankfurt, Germany

¹³Institute of Physics, Bhubaneswar 751005, India

¹⁴Indian Institute of Technology, Mumbai, India

¹⁵Indiana University, Bloomington, Indiana 47408, USA

¹⁶Alikhanov Institute for Theoretical and Experimental Physics, Moscow, Russia

¹⁷University of Jammu, Jammu 180001, India

¹⁸Joint Institute for Nuclear Research, Dubna, 141 980, Russia

¹⁹Kent State University, Kent, Ohio 44242, USA

²⁰University of Kentucky, Lexington, Kentucky, 40506-0055, USA

²¹Institute of Modern Physics, Lanzhou, China

²²Lawrence Berkeley National Laboratory, Berkeley, California 94720, USA

²³Massachusetts Institute of Technology, Cambridge, MA 02139-4307, USA

²⁴Max-Planck-Institut für Physik, Munich, Germany

- ²⁵Michigan State University, East Lansing, Michigan 48824, USA
- ²⁶Moscow Engineering Physics Institute, Moscow Russia
- ²⁷City College of New York, New York City, New York 10031, USA
- ²⁸NIKHEF and Utrecht University, Amsterdam, The Netherlands
- ²⁹Ohio State University, Columbus, Ohio 43210, USA
- ³⁰Old Dominion University, Norfolk, VA, 23529, USA
- ³¹Panjab University, Chandigarh 160014, India
- ³²Pennsylvania State University, University Park, Pennsylvania 16802, USA
- ³³Institute of High Energy Physics, Protvino, Russia
- ³⁴Purdue University, West Lafayette, Indiana 47907, USA
- ³⁵Pusan National University, Pusan, Republic of Korea
- ³⁶University of Rajasthan, Jaipur 302004, India
- ³⁷Rice University, Houston, Texas 77251, USA
- ³⁸Universidade de Sao Paulo, Sao Paulo, Brazil
- ³⁹University of Science & Technology of China, Hefei 230026, China
- ⁴⁰Shandong University, Jinan, Shandong 250100, China
- ⁴¹Shanghai Institute of Applied Physics, Shanghai 201800, China
- ⁴²SUBATECH, Nantes, France
- ⁴³Texas A&M University, College Station, Texas 77843, USA
- ⁴⁴University of Texas, Austin, Texas 78712, USA
- ⁴⁵Tsinghua University, Beijing 100084, China
- ⁴⁶United States Naval Academy, Annapolis, MD 21402, USA
- ⁴⁷Valparaiso University, Valparaiso, Indiana 46383, USA
- ⁴⁸Variable Energy Cyclotron Centre, Kolkata 700064, India
- ⁴⁹Warsaw University of Technology, Warsaw, Poland

⁵⁰University of Washington, Seattle, Washington 98195, USA

⁵¹Wayne State University, Detroit, Michigan 48201, USA

⁵²Institute of Particle Physics, CCNU (HZNU), Wuhan 430079, China

⁵³Yale University, New Haven, Connecticut 06520, USA

⁵⁴University of Zagreb, Zagreb, HR-10002, Croatia